Energies **2013**, *6*, 4830-4840; doi:10.3390/en6094830

OPEN ACCESS

energies

ISSN 1996-1073

www.mdpi.com/journal/energies

Article

Electrostatic Self-Assembly of Fe_3O_4 Nanoparticles on Graphene Oxides for High Capacity Lithium-Ion Battery Anodes

Taegyune Yoon [1], Jaegyeong Kim [1], Jinku Kim [2] and Jung Kyoo Lee [1,*]

[1] Department of Chemical Engineering, Dong-A University, Busan 604-714, Korea; E-Mails: sunny_tak@naver.com (T.Y.); worud1250@naver.com (J.K.)

[2] Department of Bio and Chemical Engineering, Hongik University, Sejong 339-701, Korea; E-Mail: jinkukim@hongik.ac.kr

* Author to whom correspondence should be addressed; E-Mail: jklee88@dau.ac.kr; Tel.: +82-51-200-7718; Fax: +82-51-200-7728.

Received: 19 July 2013; in revised form: 22 August 2013 / Accepted: 29 August 2013 / Published: 12 September 2013

Abstract: Magnetite, Fe_3O_4, is a promising anode material for lithium ion batteries due to its high theoretical capacity (924 mA h g^{-1}), high density, low cost and low toxicity. However, its application as high capacity anodes is still hampered by poor cycling performance. To stabilize the cycling performance of Fe_3O_4 nanoparticles, composites comprising Fe_3O_4 nanoparticles and graphene sheets (GS) were fabricated. The Fe_3O_4/GS composite disks of μm dimensions were prepared by electrostatic self-assembly between negatively charged graphene oxide (GO) sheets and positively charged Fe_3O_4-APTMS [Fe_3O_4 grafted with (3-aminopropyl)trimethoxysilane (APTMS)] in an acidic solution (pH = 2) followed by *in situ* chemical reduction. Thus prepared Fe_3O_4/GS composite showed an excellent rate capability as well as much enhanced cycling stability compared with Fe_3O_4 electrode. The superior electrochemical responses of Fe_3O_4/GS composite disks assure the advantages of: (1) electrostatic self-assembly between high storage-capacity materials with GO; and (2) incorporation of GS in the Fe_3O_4/GS composite for high capacity lithium-ion battery application.

Keywords: lithium-ion battery; anode; iron oxide; magnetite; graphene; self-assembly

---

1. Introduction

Lithium-ion batteries (LIBs) are being intensively pursued for the emerging large-scale applications in many electrified vehicles and energy storage system (ESS), *etc.* [1–3]. In commercial LIBs, graphitic carbon has long been used as the anode material since the first introduction of LIBs in 1991 due to its excellent cycling stability and relatively low cost. However, more advanced anode material that provides higher energy and power densities than graphitic carbon is required to meet the growing demands.

Nanostructures of iron oxides (α-Fe_2O_3 and Fe_3O_4) that store 6~8 Li ions per formula unit via electrochemical "conversion reaction" shown below have been extensively studied as potential high capacity anode materials [4–13]. They have low toxicity and high intrinsic density (5.17 g cm^{-3} for Fe_3O_4 *vs.* 2.16 g cm^{-3} for graphite), and are abundant. In spite of these highly appealing features, their use in LIB anodes is hampered by low electrical conductivity, and fast capacity fading due to severe aggregation of iron oxides particles and large volume changes inherent in the conversion reaction process [5,8,14]. Their hybridization with conductive matrices such as carbon is mostly adopted to resolve these problems. However, it is hard to get homogeneous dispersion of iron oxide nanostructures in carbon matrices. Rendering the high electrical conductivity of composites with post thermal-treatment of carbon precursors is also problematic issue due to the limited thermal stability of iron oxide nanostructures [5,9]. Among many carbon matrices, graphene is regarded as the most attractive ones because of its unique properties such as superior electrical conductivity, high thermal and chemical stability, high mechanical ductility and large surface area. Hence, graphene has been successfully used to support metal oxides including iron oxide nanostructures by employing chemical co-precipitation or solvothermal processes [7,8,15,16]:

$$Fe_2O_3 + 6Li^+ + 6e^- \leftrightarrow 2Fe^0 + 3Li_2O \quad (1)$$

$$Fe_3O_4 + 8Li^+ + 8e^- \leftrightarrow 3Fe^0 + 4Li_2O \quad (2)$$

Herein, we report an instant electrostatic self-assembly to fabricate Fe_3O_4/graphene sheets (GS) composite. For this purpose, Fe_3O_4 nanoparticles grafted with (3-aminopropyl)trimethoxysilane (Fe_3O_4-APTMS) were added into a slightly acidic dispersion of graphene oxides (GO) followed by *in situ* chemical reduction of GO. This process yielded Fe_3O_4/GS disks of μm dimensions in which Fe_3O_4 nanoparticles are in intimate contacts with GS and are ideally dispersed between GS layers. As an anode material for LIB, the Fe_3O_4/GS composite disks with unique morphology exhibited a high reversible discharge capacity of 674 mA h g^{-1} at 100 mA g^{-1} with an excellent cycling stability up to 100 cycles. The Fe_3O_4/GS disks also showed high rate capability, *i.e.*, ~300 mA h g^{-1} at the current as high as 2000 mA g^{-1}.

2. Results and Discussion

Scheme 1 illustrates the electrostatic self-assembly process between Fe_3O_4-APTMS and GO to prepare Fe_3O_4/GS composite disks. In an acidic solution, the positively charged Fe_3O_4-APTMS is homogeneously bound on the surface of negatively charged GO sheets by instant electrostatic interactions. The Fe_3O_4/GO composite was subsequently reduced *in situ* with hydrazine to give Fe_3O_4/GS composite disks.

Scheme 1. Schematic diagram for the electrostatic self-assembly process.

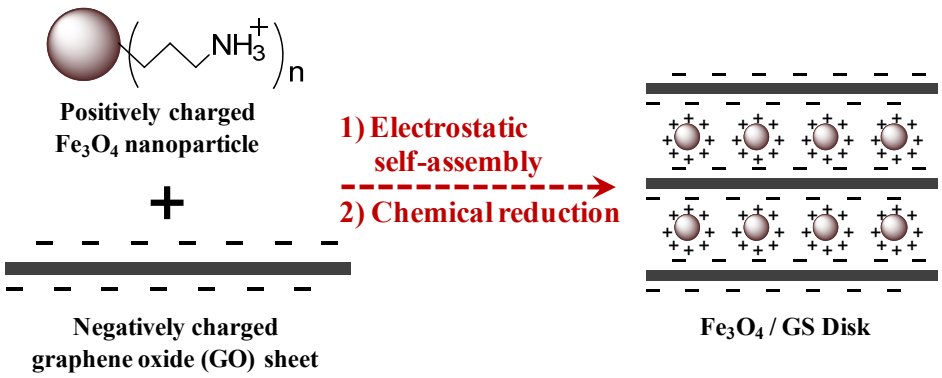

Figure 1a compares the Fourier transform infrared spectroscopy (FTIR) spectra of Fe_3O_4 and Fe_3O_4-APTMS. In the spectrum of Fe_3O_4, a strong band at 500–700 cm^{-1} due to the Fe–O stretching vibration and a broad band at 3400–3600 cm^{-1} due to the stretching vibration of the surface –OH groups of Fe_3O_4 was observed [17,18]. The surface –OH groups attack the labile methoxy-groups in APTMS to form Fe–O–Si bonds at elevated temperature. Different from the spectrum of bare Fe_3O_4, that of Fe_3O_4-APTMS clearly showed the stretching vibration band of Si–O bonds in Fe–O–Si at 1050–1100 cm^{-1} with the stretching vibration bands of C–H in alkyl chains at 2850 cm^{-1}, 2925 cm^{-1} and 2956 cm^{-1}. The bands at 3423 cm^{-1} and 1635 cm^{-1} correspond to N–H stretching and bending vibrations in free amines, respectively, and the band at 1385 cm^{-1} corresponds to C–N stretching vibration. The FTIR spectrum of Fe_3O_4-APTMS indicates that the surfaces of Fe_3O_4 nanoparticles were successfully grafted with APTMS. As shown in Figure 1b, the X-ray diffraction (XRD) patterns of Fe_3O_4 nanoparticles and Fe_3O_4/GS composite disks match well with that of magnetite (JCPDS No. 19-0629). With the Scherrer's formula, $D = 0.89\lambda/(\beta\cos\theta)$, to the line width of (311) diffraction, the average particle size of Fe_3O_4 was estimated to be 10.1 nm. The magnetite structure was preserved in the Fe_3O_4/GS composite after *in situ* chemical reduction with hydrazine.

Figure 1. (**a**) Fourier transform infrared spectroscopy (FTIR) spectra: (i) Fe_3O_4 and (ii) Fe_3O_4-APTMS; (**b**) X-ray diffraction (XRD) patterns: (i) Fe_3O_4 and (ii) Fe_3O_4/GS [inset is the XRD patterns of graphene oxides (GO) and reduced GO (rGO)].

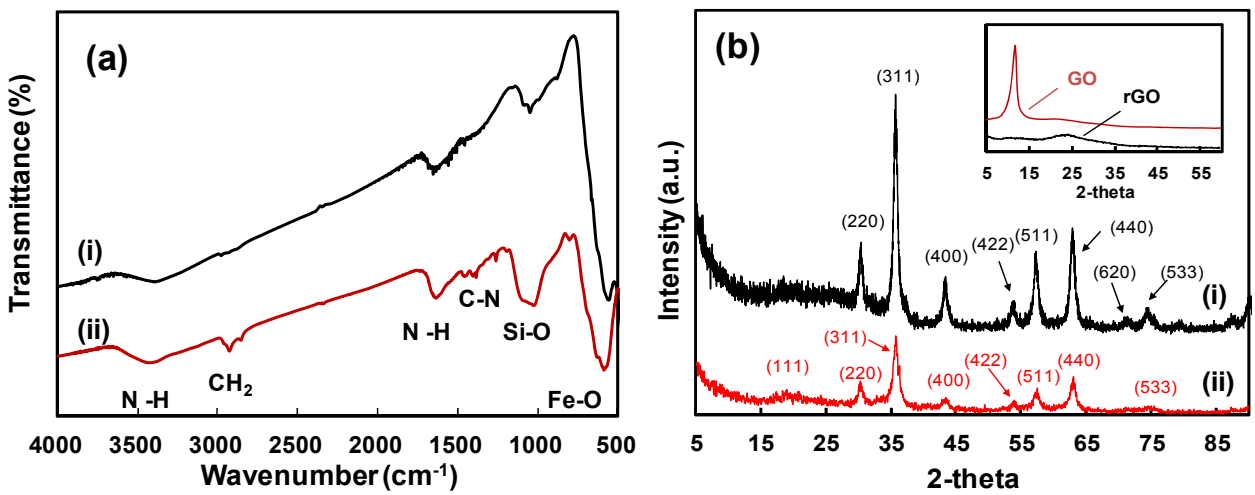

Figure 2 presents photographs of GO and Fe_3O_4-APTMS dispersions in acidic solution, and hydrazine-reduced Fe_3O_4/GS. GO and Fe_3O_4-APTMS formed homogeneous dispersions by sonication in acidic solution as shown in Figure 2a,b, respectively. Right after the two dispersions are mixed together, Fe_3O_4/GO aggregates were precipitated due to electrostatic assembly. After addition of hydrazine, the reduced Fe_3O_4/GS composite floated to the surface of clear solution (Figure 2c), indicating hydrophobic nature of composite surface and complete electrostatic assembly between Fe_3O_4-APTMS and GO sheets.

Figure 2. Photographs: (**a**) GO dispersion; (**b**) Fe_3O_4-APTMS dispersion; and (**c**) reduced Fe_3O_4/GS solution.

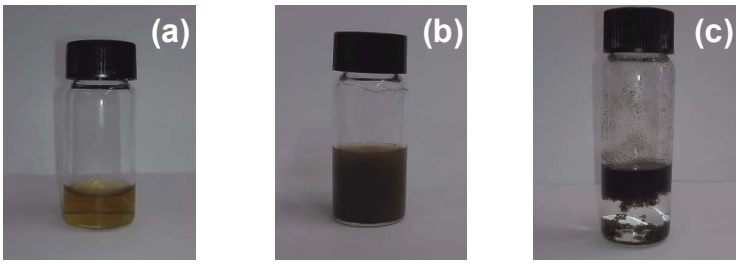

Figure 3 shows X-ray photoelectron spectroscopy (XPS) spectrum of Fe_3O_4/GS composite. Insets are the high-resolution spectra of the Si_{2p} (left) and C_{1s} (right) regions. A small Si_{2p} peak with binding energy of 102.0 eV was detected, providing additional evidence of successful grafting of APTMS on Fe_3O_4 [17]. The two Fe peaks with binding energies of 710.9 eV and 724.4 eV were attributed to $Fe_{2p3/2}$ and $Fe_{2p1/2}$, respectively, for trivalent Fe in the Fe_3O_4. The C_{1s} spectra showed an intense peak at 284.6 eV due to the C–C bonds in GS with substantially low peak intensities assignable to the C–O moieties in pristine GO, supporting high degree of GO reduction with hydrazine [19].

Figure 3. X-ray photoelectron spectroscopy (XPS) spectrum of Fe_3O_4/GS composite. Insets are the high-resolution spectra of Si_{2p} and C_{1s} regions.

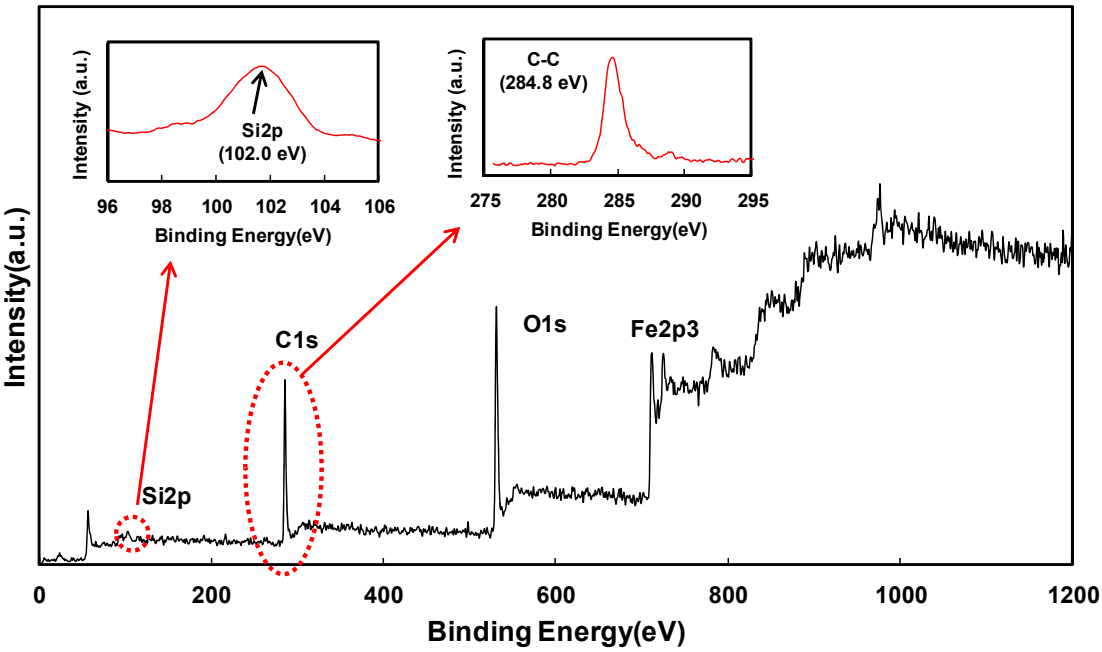

The amount of Fe_3O_4 in the composite was estimated to be 54.5 wt% by thermogravimetric analysis (TGA) profile shown in Figure 4a, for which mass loss below 200 °C was assumed to be adsorbed water. The scanning electron microscopy (SEM) image of Fe_3O_4/GS composites in Figure 4b, showed disk-shaped aggregates of 1–3 μm in size with thicknesses of 0.5–1 μm. The size of composite disks is comparable to that of pristine flake graphite used to prepare GO. The structure of Fe_3O_4/GS composite was further investigated by transmission electron microscopy (TEM). As shown in Figure 4c, Fe_3O_4 nanoparticles with a size range of 10–20 nm are dispersed on GS and are in close contact with very thin layers of GS. The lattice *d*-spacings of 0.47 nm, 0.297 nm and 0.25 nm corresponding to (111), (220) and (311) planes of Fe_3O_4, respectively, were identified in the high resolution TEM image (Figure 4d).

Figure 4. (**a**) Thermogravimetric analysis (TGA) profile; (**b**) scanning electron microscopy (SEM) image; (**c**) and (**d**) transmission electron microscopy (TEM) images of Fe_3O_4/GS composite.

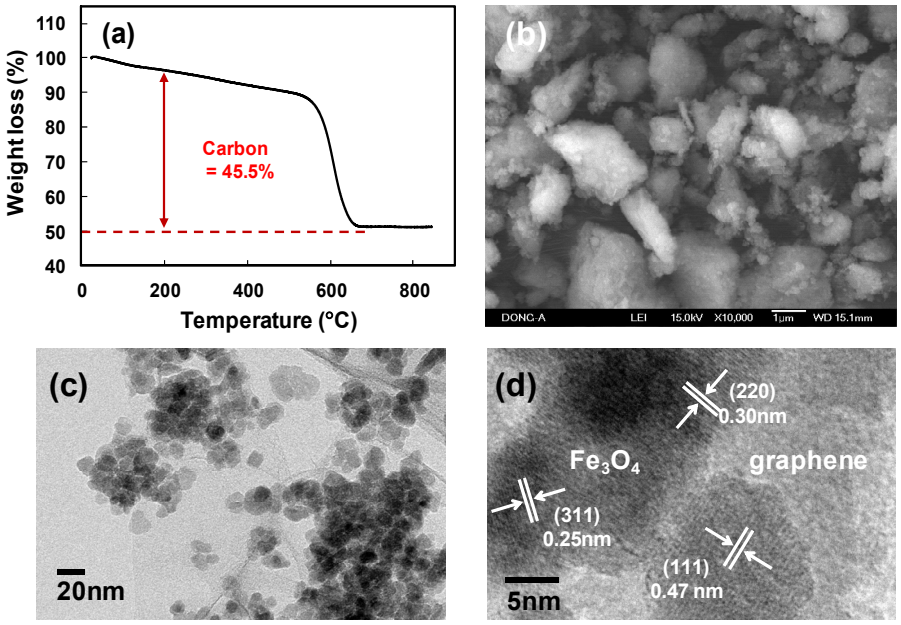

The electrochemical properties of Fe_3O_4/GS composite were tested in comparison to those of Fe_3O_4 nanoparticles by cyclic voltammetry (CV) and galvanostatic cycling tests. Figure 5a,b shows the CV curves for the initial five cycles. In the first cathodic scan of Fe_3O_4 electrode, a strong reduction peak was observed at 0.55 V due to the electrochemical reduction of Fe^{3+} and Fe^{2+} to Fe^0 [9,20,21]. In the subsequent cycles, the obvious peak at 0.55 V was shifted to 0.6–0.7 V due to the polarization. In the first anodic scan, two broad peaks were recorded at 1.72 V and 1.82 V assignable to the oxidation of Fe^0 to Fe^{2+} and Fe^{3+}, respectively [8,14,21]. In the subsequent cycles, however, the peak at 1.82 V is hardly observed indicating the redox cycle between Fe^0 and Fe^{2+} would be the major process. Overall, the integrated areas of both cathodic and anodic scans of Fe_3O_4 electrode were substantially decreased in five cycles, indicating electrochemical irreversibility. Figure 5b shows much stabilized CV responses for the Fe_3O_4/GS composite. The major cathodic and anodic peaks were recorded at 0.65 V and 1.67/1.81 V, respectively. The Fe_3O_4/GS showed much less polarization after the first scan than Fe_3O_4 alone and the CV curves of subsequent cycles almost overlapped indicating excellent

electrochemical reversibility. In particular, in the Fe_3O_4/GS composite, two anodic peaks at 1.67 V and 1.81 V due to Fe^0 oxidation to Fe^{2+} and Fe^{3+}, respectively, were repeatedly observed. The voltage difference between cathodic and anodic process was also decreased in comparison to that of Fe_3O_4 alone possibly due to the enhanced conductivity in Fe_3O_4/GS. Figure 5c,d presents the voltage-capacity profiles of Fe_3O_4 nanoparticles and Fe_3O_4/GS composite, respectively, for the initial five cycles at a current density of 100 mA g^{-1}. In the first discharge curves, both electrodes showed long voltage plateaus at around 0.8 V *vs.* Li^+/Li due to the reduction of Fe^{3+} and Fe^{2+} to Fe^0 followed by downward sloping voltage profiles due to the combined effects of the formation of solid electrolyte interphase (SEI) layers and possibly interfacial lithium storage [8,22]. In the first charge profiles, both electrodes showed sloping voltage plateaus in 1.25–2.0 V mainly due to the oxidation of Fe^0 to Fe^{2+} and Fe^{3+}. After the first cycle, the charge and discharge capacities of Fe_3O_4 decreased rapidly with cycling while those of Fe_3O_4/GS were maintained at around 700 mA h g^{-1}.

Figure 5. Cyclic voltammetry (CV) curves of (**a**) Fe_3O_4 and (**b**) Fe_3O_4/GS; voltage profiles of (**c**) Fe_3O_4 and (**d**) Fe_3O_4/GS cycled at the current of 100 mA g^{-1}.

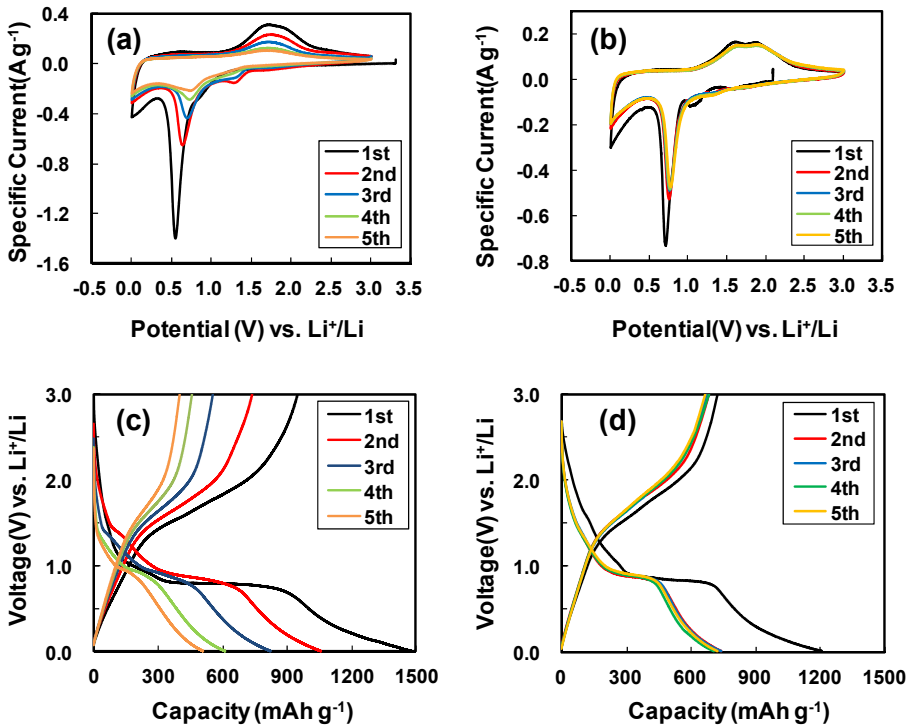

As shown in Figure 6, the Fe_3O_4 electrode exhibited very high discharge and charge capacities of 1478 mA h g^{-1} and 949 mA h g^{-1} in the first cycle, respectively, resulting in a coulombic efficiency (CE) of 64.2%. However, it lost most of its capacity after ten cycles and delivered less than 200 mA h g^{-1} at the 50th cycle. On the other hand, Fe_3O_4/GS composite showed much enhanced cycling stability. The initial discharge and charge capacities of Fe_3O_4/GS were 1126 mA h g^{-1} and 674 mA h g^{-1}, respectively, corresponding to the CE of 59.9%. In the following cycles, the reversible discharge capacity was more than 600 mA h $g^{-1}$and the capacity retention at the 100th cycle was about 80%. The GS electrode delivered the reversible capacity on the order of 200 mA h g^{-1}. Of the capacity (674 mA h g^{-1}) of Fe_3O_4/GS, the contribution by the GS is estimated to be 91 mA h g^{-1} (13.5%) considering that the weight fractions of Fe_3O_4 and GS equal to 55.5% and 45.5%, respectively.

Hence, Fe_3O_4 in the composite delivered about 583 mA h g^{-1}, which was slightly larger than the one calculated with its theoretical capacity (924 mA h g^{-1} × 55.5% = 513 mA h g^{-1}) possibly due to the interfacial lithium storage [8,22].

Figure 6. Cycling performances of GS, Fe_3O_4 and Fe_3O_4/GS at the current of 100 mA g^{-1}. Open and filled symbols denote discharge and charge capacities, respectively.

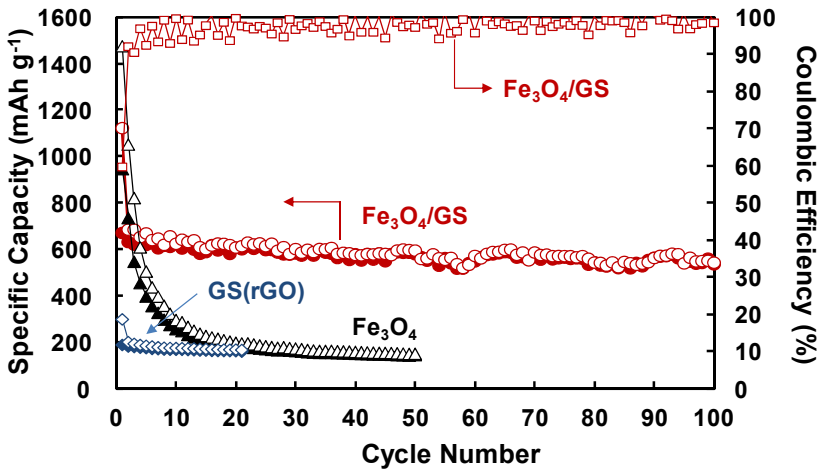

The Fe_3O_4/GS also exhibited excellent rate performances, as shown in Figure 7. On average, the capacity retentions at 500 mA g^{-1}, 1000 mA g^{-1} and 2000 mA g^{-1} were about 78%, 61% and 57% of the capacity at 100 mA g^{-1}. When the current was returned back to 100 mA g^{-1} after 45 cycles, the initial capacity was completely recovered, indicating an excellent electrochemical reversibility of Fe_3O_4/GS. The enhanced electrochemical responses of Fe_3O_4/GS compared with unsupported Fe_3O_4 could be attributed to the combined effects: (1) the high dispersion of Fe_3O_4 nanoparticles on GS layers by employing the electrostatic self-assembly method, which suppresses the agglomeration of metal oxide particles and the consequential capacity fade upon cycling; (2) the flexible and electrically conductive nature of GS layers that accommodates mechanical stresses inherent in the conversion reaction of Fe_3O_4 and maintains electrically conductive-networks through the electrode; and (3) relatively high wettability of electrolytes in the layers between Fe_3O_4 nanoparticles and GS, which can result in enhanced rate capability.

Figure 7. Rate performances of Fe_3O_4/GS.

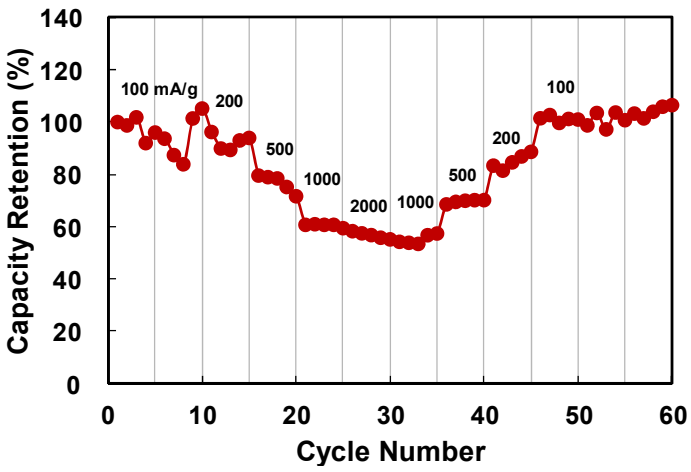

3. Experimental Section

3.1. Synthesis of Fe_3O_4 Nanoparticles and GO

Fe_3O_4 nanoparticles were synthesized by the hydrothermal liquid-interface reaction in the literatures [8,9]. In a 20 mL glass vial, $Fe(NO_3)_3 \cdot 9H_2O$ (0.40 g) was dissolved in ethylene glycol (EG, 5 mL). The vial was placed into a 30 mL Teflon autoclave that contained 28% ammonia solution (5.3 mL). The autoclave was sealed and placed in a furnace. The furnace was heated to 180 °C for 12 h. After cooling, the powder was washed with ethanol by centrifugation and filtration for several times. GO was synthesized by the modified Hummers method with commercial flake graphite (230 U Grade, Asbury Carbons, Asbury, NJ, USA) [23–25]. The GO was diluted to make a ~6% *w*/*w* in water and was subjected to sonication to get an aqueous dispersion of GO sheets.

3.2. Preparation of Fe_3O_4-APTMS and Fe_3O_4/GS Composite

Fe_3O_4 nanoparticles (0.1 g) were dispersed into dry toluene (10 mL) via sonication in an argon-filled flask. After 30 min, APTMS (0.1 mL) was poured into the solution and refluxed for 24 h under a N_2 atmosphere and washed with ethanol by centrifugation and filtration to obtain amine-functionalized Fe_3O_4 nanoparticles (Fe_3O_4-APTMS). Fe_3O_4-APTMS powder (0.1 g) was re-dispersed in ethanol (100 mL). The pH values of Fe_3O_4-APTMS dispersion in ethanol and GO dispersion in water were adjusted to be around 2 by adding appropriate amount of hydrochloric acid solution. An acidic condition was employed to make sure that the surface of APTMS-Fe_3O_4 is rendered with positive charge [26]. The Fe_3O_4/GS composite was fabricated via electrostatic self-assembly between positively charged Fe_3O_4-APTMS and negatively charged GO in acidic solution (pH = 2), followed by chemical reduction with hydrazine. Fe_3O_4-APTMS solution (0.50 mg mL^{-1}, 200 mL, pH = 2) was added into aqueous GO solution (0.18 mg mL^{-1}, 125 mL, pH = 2) under stirring. After stirring for 1 h, a small amount of hydrazine solution (35 wt% in water) was added into the obtained dark brownish solution under stirring. The self-assembled composites were further reduced overnight at room temperature. The supernatant was decanted and resulting black dispersion was washed with distilled water for several times and dried at 80 °C overnight to obtain the Fe_3O_4/GS powder. For comparison, GS (rGO) sample was prepared by hydrazine reduction of GO.

3.3. Materials Characterization

FTIR spectra were collected on a Nicolet 380 spectrometer using wafers formed by mixing the sample (2–3 wt%) with KBr powder and then pelletized. The powder XRD patterns of samples were recorded on an Ultima IV, Rigaku model D/MAX-50 kV system (Cu-K_α radiation, λ = 1.5418 Å). XPS was performed on a Thermo Electron Corporation spectrometer with an Al K_α (1486.6 eV) radiation. The carbon content in Fe_3O_4/GS was determined by the weight loss in a TGA run to 800 °C at a ramping rate of 10 °C min^{-1} in an air flow. The morphology of Fe_3O_4/GS was investigated by using SEM (JEOL JSM-35CF operated at 10.0 kV, JEOL Ltd., Tokyo, Japan) and TEM (JEOL JEM-2010 operated at 200.0 kV, JEOL Ltd., Tokyo, Japan).

3.4. Electrochemical Measurements

Electrochemical tests were conducted using R-2032 coin cell with Li foil as the counter-electrode. The working electrodes (35–40 μm thick) were prepared by casting a paste consisting of 80 wt% active material [Fe_3O_4 nanoparticles, GS (rGO) or Fe_3O_4/GS composite], 10 wt% conductive additive (Super P-Li, TIMCAL Ltd., Bodio, Switzerland) and 10 wt% poly(vinylidene fluoride) (PVDF) binder onto a copper foil. The typical mass loading of the working electrode was 2.5–3.0 mg cm^{-2}. A polypropylene membrane (Celgard 2400) was used as the separator. 1.0 M $LiPF_6$ in an ethylene carbonate/dimethyl carbonate/diethyl carbonate (EC/DMC/DEC) mixture (3:4:3 *v*/*v*/*v*) provided by Panax Etech Ltd. (Busan, Korea) was used as the electrolyte. The cells were assembled in an argon-filled glove box. Cyclic voltammograms were recorded in the voltage range of 3.0–0.01 V *vs.* Li^+/Li at 0.1 mV s^{-1}. The cells were galvanostatically cycled in the cut-off voltage range of 3.0–0.01 V *vs.* Li^+/Li using a galvanostat/potentiostat system (WonATech, Seoul, Korea).

4. Conclusions

Fe_3O_4/GS composite disks, in which Fe_3O_4 nanoparticles were ideally dispersed in GS layers, were prepared by electrostatic self-assembly of positively charged Fe_3O_4-APTMS nanoparticles on negatively charged GO sheets in acidic aqueous solution followed by *in situ* chemical reduction. Thus prepared Fe_3O_4/GS composite showed an excellent rate capability as well as much enhanced cycling stability compared with Fe_3O_4 electrode. The superior electrochemical responses of Fe_3O_4/GS composite disks assure the advantages of: (1) electrostatic self-assembly between high storage-capacity materials with GO sheets, and (2) the incorporation of GS in the Fe_3O_4/GS composite for high capacity LIB application.

Acknowledgments

This work was supported by the Dong-A University Research Fund.

Conflicts of Interest

The authors declare no conflict of interest.

References

1. Tarascon, J.M. Key challenges in future Li-battery research. *Philos. Trans. R. Soc. A Math. Phys. Eng. Sci.* **2010**, *368*, 3227–3241.
2. Hassoun, J.; Lee, K.S.; Sun, Y.K.; Scrosati, B. An advanced lithium ion battery based on high performance electrode materials. *J. Am. Chem. Soc.* **2011**, *133*, 3139–3143.
3. Thackeray, M.M.; Wolverton, C.; Isaacs, E.D. Electrical energy storage for transportation—Approaching the limits of, and going beyond, lithium-ion batteries. *Energy Environ. Sci.* **2012**, *5*, 7854–7863.
4. Poizot, P.; Laruelle, S.; Grugeon, S.; Dupont, L.; Tarascon, J.M. Nano-sized transition-metal oxides as negative-electrode materials for lithium-ion batteries. *Nature* **2000**, *407*, 496–499.

5. Zhang, W.M.; Wu, X.L.; Hu, J.S.; Guo, Y.G.; Wan, L.J. Carbon coated Fe_3O_4 nanospindles as a superior anode material for lithium-ion batteries. *Adv. Funct. Mater.* **2008**, *18*, 3941–3946.
6. Cabana, J.; Monconduit, L.; Larcher, D.; Palacin, M.R. Beyond intercalation-based Li-ion batteries: The state of the art and challenges of electrode materials reacting through conversion reactions. *Adv. Mater.* **2010**, *22*, E170–E192.
7. Zhou, G.M.; Wang, D.W.; Li, F.; Zhang, L.L.; Li, N.; Wu, Z.S.; Wen, L.; Lu, G.Q.; Cheng, H.M. Graphene-wrapped Fe_3O_4 anode material with improved reversible capacity and cyclic stability for lithium ion batteries. *Chem. Mater.* **2010**, *22*, 5306–5313.
8. Lian, P.C.; Zhu, X.F.; Xiang, H.F.; Li, Z.; Yang, W.S.; Wang, H.H. Enhanced cycling performance of Fe_3O_4-graphene nanocomposite as an anode material for lithium-ion batteries. *Electrochim. Acta* **2010**, *56*, 834–840.
9. Yoon, T.; Chae, C.; Sun, Y.K.; Zhao, X.; Kung, H.H.; Lee, J.K. Bottom-up *in situ* formation of Fe_3O_4 nanocrystals in a porous carbon foam for lithium-ion battery anodes. *J. Mater. Chem.* **2011**, *21*, 17325–17330.
10. Hassoun, J.; Croce, F.; Hong, I.; Scrosati, B. Lithium-iron battery: Fe_2O_3 anode *versus* $LiFePO_4$ cathode. *Electrochem. Commun.* **2011**, *13*, 228–231.
11. Ji, L.W.; Lin, Z.; Alcoutlabi, M.; Zhang, X.W. Recent developments in nanostructured anode materials for rechargeable lithium-ion batteries. *Energy Environ. Sci.* **2011**, *4*, 2682–2699.
12. Ji, L.W.; Tan, Z.K.; Kuykendall, T.R.; Aloni, S.; Xun, S.D.; Lin, E.; Battaglia, V.; Zhang, Y.G. Fe_3O_4 nanoparticle-integrated graphene sheets for high-performance half and full lithium ion cells. *Phys. Chem. Chem. Phys.* **2011**, *13*, 7139–7146.
13. Ji, L.W.; Toprakci, O.; Alcoutlabi, M.; Yao, Y.F.; Li, Y.; Zhang, S.; Guo, B.K.; Lin, Z.; Zhang, X.W. α-Fe_2O_3 nanoparticle-loaded carbon nanofibers as stable and high-capacity anodes for rechargeable lithium-ion batteries. *ACS Appl. Mater. Interfaces* **2012**, *4*, 2672–2679.
14. He, Y.; Huang, L.; Cai, J.S.; Zheng, X.M.; Sun, S.G. Structure and electrochemical performance of nanostructured Fe_3O_4/carbon nanotube composites as anodes for lithium ion batteries. *Electrochim. Acta* **2011**, *55*, 1140–1144.
15. Zhu, X.J.; Zhu, Y.W.; Murali, S.; Stollers, M.D.; Ruoff, R.S. Nanostructured reduced graphene oxide/Fe_2O_3 composite as a high-performance anode material for lithium ion batteries. *ACS Nano* **2011**, *5*, 3333–3338.
16. Wang, H.L.; Cui, L.F.; Yang, Y.A.; Casalongue, H.S.; Robinson, J.T.; Liang, Y.Y.; Cui, Y.; Dai, H.J. Mn_3O_4-graphene hybrid as a high-capacity anode material for lithium ion batteries. *J. Am. Chem. Soc.* **2010**, *132*, 13978–13980.
17. Reddy, K.R.; Lee, K.P.; Gopalan, A.Y.; Kang, H.D. Organosilane modified magnetite nanoparticles/poly(aniline-co-o/m-aminobenzenesulfonic acid) composites: Synthesis and characterization. *React. Funct. Polym.* **2007**, *67*, 943–954.
18. Seckin, T.; Vural, S.; Koytepe, S. Preparation and structural properties of Fe_3O_4-polyimide hybrid nanocomposites. *Polym. Bull.* **2010**, *64*, 115–126.
19. Stankovich, S.; Dikin, D.A.; Piner, R.D.; Kohlhaas, K.A.; Kleinhammes, A.; Jia, Y.; Wu, Y.; Nguyen, S.T.; Ruoff, R.S. Synthesis of graphene-based nanosheets via chemical reduction of exfoliated graphite oxide. *Carbon* **2007**, *45*, 1558–1565.

20. Chun, L.; Wu, X.Z.; Lou, X.M.; Zhang, Y.X. Hematite nanoflakes as anode electrode materials for rechargeable lithium-ion batteries. *Electrochim. Acta* **2010**, *55*, 3089–3092.
21. Jin, S.L.; Deng, H.G.; Long, D.H.; Liu, X.J.; Zhan, L.A.; Liang, X.Y.; Qiao, W.M.; Ling, L.C. Facile synthesis of hierarchically structured Fe_3O_4/carbon micro-flowers and their application to lithium-ion battery anodes. *J. Power Sources* **2011**, *196*, 3887–3893.
22. Wu, X.L.; Guo, Y.G.; Wan, L.J.; Hu, C.W. α-Fe_2O_3 nanostructures: Inorganic salt-controlled synthesis and their electrochemical performance toward lithium storage. *J. Phys. Chem. C* **2008**, *112*, 16824–16829.
23. Kovtyukhova, N.I.; Ollivier, P.J.; Martin, B.R.; Mallouk, T.E.; Chizhik, S.A.; Buzaneva, E.V.; Gorchinskiy, A.D. Layer-by-layer assembly of ultrathin composite films from micron-sized graphite oxide sheets and polycations. *Chem. Mater.* **1999**, *11*, 771–778.
24. Lee, J.K.; Smith, K.B.; Hayner, C.M.; Kung, H.H. Silicon nanoparticles-graphene paper composites for Li ion battery anodes. *Chem. Commun.* **2010**, *46*, 2025–2027.
25. Yoon, T.; Cho, M.; Suh, Y.W.; Oh, E.S.; Lee, J.K. Reassembled graphene-platelets encapsulated silicon nanoparticles for Li-ion battery anodes. *J. Nanosci. Nanotech.* **2011**, *11*, 10193–10200.
26. Yang, S.B.; Feng, X.L.; Ivanovici, S.; Mullen, K. Fabrication of graphene-encapsulated oxide nanoparticles: Towards high-performance anode materials for lithium storage. *Angew. Chem. Int. Ed.* **2010**, *49*, 8408–8411.